Achievement of Ultralow Elastic Modulus through Optimization of Phase Stability and Recrystallization Texture in Ti–Nb–Fe–Sn Alloys

Muhammad Farzik Ijaz, Wataru Tasaki, Hee Young Kim, and Shuichi Miyazaki*

Ti–Nb–Fe–Sn alloys with relatively low Nb content, located near the phase boundary of $(\beta+\omega)/\beta$, are designed on the basis of electron-to-atom (e/a) ratio, d-electron alloy design concept, and Mo equivalent (Mo_{eq}) aiming at low Young's modulus comparable to human bone. The effect of Sn content and Nb content on the microstructure and the mechanical properties is investigated in Ti–5Nb–3Fe–(0–6)Sn (at%) and Ti–(3–9)Nb–3Fe–4Sn (at%) alloys. The composition dependence of Young's modulus and tensile strength of Ti–Nb–Fe–Sn alloys is analyzed in terms of the phase stability, ω phase, and recrystallization texture. Both Nb and Sn are effective in suppressing the athermal ω phase and stabilizing the β phase. The recrystallization texture is strongly influenced by the content of Sn and Nb. A strong $\{110\}_\beta\langle 001\rangle_\beta$ Goss texture is formed in the Ti–5Nb–3Fe–(2–4)Sn and Ti–(3–5)Nb–3Fe–4Sn alloys. The Ti–5Nb–3Fe–4Sn alloy exhibits an exceptionally low Young's modulus of 30 GPa due to the combined effects of low stability of the β phase, a small amount of ω phase, and a strong Goss texture.

1. Introduction

Ti and its alloys have been considered to be indispensable materials for biomedical applications due to their suitable combination of physical and mechanical properties such as high specific strength, low modulus, high corrosion resistance, and excellent biocompatibility.[1,2] Most importantly, Young's modulus of Ti alloys is less than half of those of the stainless steels and Co-based alloys, making them more reliable in a wide range of implant applications.[3–5] However, Young's modulus value of $(\alpha+\beta)$-type Ti–6Al–4 V (≈110 GPa), which is the most commonly used Ti alloy, is still much higher than that of human bone (10–30 GPa).[1–5] This large discrepancy in Young's moduli at the human bone/implant interface can generate "stress shielding", leading to bone resorption and delayed bone healing.[5,6]

Over the past decades, extensive efforts have been made to develop biomedical Ti alloys with low Young's modulus as close as possible to that of the surrounding bone tissues. As a result, several promising β-type Ti alloys have been developed by adjusting alloying elements and/or thermomechanical processing routes.[7–32] However, Young's modulus of most reported β-type Ti alloys is typically in the range of 50–80 GPa, so further reduction is desirable to approach Young's modulus of human bone. Young's modulus of β-type Ti alloys is influenced by multiple factors, including the stability of the β phase, the formation of the ω phase, and the texture. It has been widely acknowledged that the stability of the β phase is the most important factor.[12,14,19,33–39] Young's modulus decreases as the stability of the β phase decreases; however, the decrease in the stability of the β phase leads to the formation of the ω phase or the α'' martensite phase, which have higher Young's modulus. Therefore, Young's modulus is minimized at the compositions locating near the phase boundary of $(\beta+\alpha'')/\beta$ or $(\beta+\omega)/\beta$.[8,12,30,37] Young's modulus is also strongly dependent on the orientation of the crystals; therefore, texture is one of the key factors affecting Young's modulus of β-type Ti alloys. It has been well documented that the modulus is the lowest along the $\langle 100\rangle$ direction in β-type Ti alloys.[34,38,39] Recently, it has been reported that very low Young's moduli in the range of 31.5–44 GPa can be achieved in Ti–Mo–Al–Zr, Ti–Zr–Nb–Sn–Mo, and Ti–Nb–Sn alloys by the formation of Goss texture of $\{110\}_\beta\langle 001\rangle_\beta$.[40–42] In particular, a bone-like elastic modulus of 31.5 GPa was achieved in a Ti–15Nb–5.5Sn (at%) alloy due to the formation of a strong $\{110\}_\beta\langle 001\rangle_\beta$ texture and the suppression of the α'' martensite phase and ω phase.[42]

On the other hand, most β-type titanium alloys contain large amounts of elements with high cost and high density such as Nb, Ta, Mo, and Zr to stabilize the β phase. To combat this problem,

---

M. F. Ijaz
Mechanical Engineering Department
College of Engineering
King Saud University
P.O. Box 800, Riyadh 11421, Saudi Arabia

M. F. Ijaz
Graduate School of Pure and Applied Sciences
University of Tsukuba
Tsukuba, Ibaraki 305-8573, Japan

W. Tasaki, H. Y. Kim, S. Miyazaki
Division of Materials Science
Faculty of Pure and Applied Sciences
University of Tsukuba
Tsukuba, Ibaraki 305-8573, Japan
E-mail: heeykim@ims.tsukuba.ac.jp

The ORCID identification number(s) for the author(s) of this article can be found under https://doi.org/10.1002/adem.202300468.

DOI: 10.1002/adem.202300468

low-cost elements such as Fe, Mn, and Cr have attracted attention as β phase stabilizing elements. For example, Ti–Nb–Fe–Sn, Ti–Nb–Fe–Zr, and Ti–Nb–Fe–Cr alloys are developed as low-cost biomedical Ti alloys.[43–46] However, Young's modulus of these alloys is still higher than 50 GPa. In this study, Ti–Nb–Fe–Sn alloys with relatively low Nb content were designed and optimized to achieve low Young's modulus comparable to human bone. In particular, the effects of Sn content and Nb content on the microstructure and the mechanical properties were investigated in Ti–5Nb–3Fe–(0–6)Sn (at%) and Ti–(3–9)Nb–3Fe–4Sn (at%) alloys, respectively. The composition dependence of Young's modulus and tensile strength in Ti–Nb–Fe–Sn alloys was analyzed in terms of the phase stability, ω phase, and recrystallization texture.

2. Experimental Section

2.1. Alloy Design

Three representative approaches, that is, electron-to-atom (e/a) ratio, d-electron alloy design theory, and Mo equivalent (Mo_{eq}), were considered in this study. The *d*-electron alloy design theory is based on molecular orbital calculations of the electronic structure using two parameters of the bond order (*Bo*) and the d-orbital energy level (*Md*), where *Bo* is a measure of the covalent bond strength between Ti and the alloying element and *Md* is found to be closely related to the electronegativity and atomic radius of each alloying element. For multicomponent alloys, compositional averages of *Bo* and *Md* were used. The *Bo*–*Md* diagram was successfully utilized to predict phase boundaries and deformation mechanisms in Ti alloys.[47–50] **Figure 1** shows the *Bo*–*Md* diagram displaying the regions of α, α + β and β alloys proposed by Morinaga et al.[47] In general, the β phase becomes unstable with decreasing *Bo* and with increasing *Md*. The primary aim of this study was to explore possibilities of a Ti–Nb–Fe–Sn system with low Nb content less than 10 at% as low-cost biomedical Ti alloys. In this study, two series of alloys, that is, Ti–(3–9)Nb–3Fe–4Sn (at%) and Ti–5Nb–3Fe–(0–6)Sn (at%) alloys, which were located near the phase boundary of (β + α″)/β were designed. Fe was selected for its strong β stabilizing effect in Ti alloys and low cost. The amount of Fe was determined to be 3 at% in order to reduce the Nb content less than 10 at%. Sn was selected to suppress the ω phase while maintaining low e/a ratio. The Ti–(3–9)Nb–3Fe–4Sn (at%) and Ti–5Nb–3Fe–(0–6)Sn (at%) alloys are denoted in Figure 1 as solid circles and solid squares, respectively.

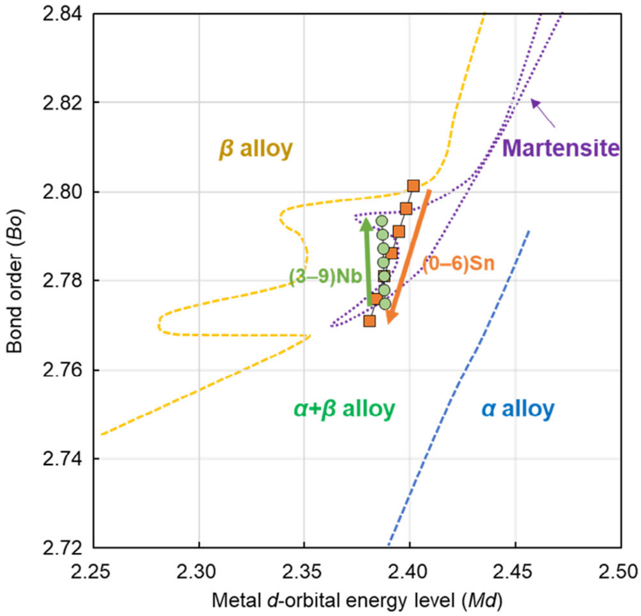

Figure 1. *Bo*–*Md* diagram showing the positions of the designed alloys in this study.

It was well established that Young's modulus decreased with decreasing e/a ratio in β-Ti alloys in so far as the β phase was maintained and the formation of the ω phase was suppressed.[12,14,19,33–39] It was reported that the lower limit of the e/a ratio to maintain the β phase for Ti–Nb binary alloys was about 4.25.[8,37] In multicomponent alloys, such as Ti–Nb–Zr, Ti–Nb–Sn, and Ti–Nb–Zr–Sn, the lower limit of e/a to maintain the β phase was reduced to about 4.15 and then very low Young's modulus <60 GPa can be achieved.[12,19,30,41,42] This is due to the fact that the addition of Zr or Sn did not change the e/a value of Ti alloys, although they suppressed the martensitic transformation from the β phase to the α″ phase in Ti–Nb alloys. On the other hand, the molybdenum equivalent (Mo_{eq}) was useful to assess the β phase stability of Sn or Zr-contained alloys.[42,51] In this study, a modified Mo_{eq} proposed by Wang et al. ($[Mo_{eq}] = [Mo] + 0.28[Nb] + 1.93[Fe] + 0.30[Sn] + \ldots$ (wt%)) was used to evaluate the β phase stability.[51] Wang et al. claimed that the Mo_{eq} values of β–Ti alloys with lower Young's moduli in the range of 40–70 GPa were close to the critical Mo_{eq} value of 11.8 wt% Mo.[51] The compositional average values of *Bo* and *Md*, e/a ratio values, and Mo_{eq} values of the alloys designed in this study are listed in **Table 1**. It is worth noting that the Mo_{eq} and e/a ratio for all the designed alloys were very close to the lower limits for maintaining the β phase.

Table 1. Alloy compositions investigated in this study and their *Bo*, *Md*, e/a, and molybdenum equivalent (Mo_{eq}) values.

Alloy [at%]	*Bo*	*Md*	e/a	Mo_{eq} [wt%]
Ti–5Nb–3Fe	2.8013	2.4015	4.17	9.00
Ti–5Nb–3Fe–1Sn	2.7962	2.3980	4.17	9.58
Ti–5Nb–3Fe–2Sn	2.7911	2.3946	4.17	10.13
Ti–5Nb–3Fe–3Sn	2.7861	2.3911	4.17	10.67
Ti–5Nb–3Fe–4Sn	2.7810	2.3876	4.17	11.20
Ti–5Nb–3Fe–5Sn	2.7759	2.3842	4.17	11.72
Ti–5Nb–3Fe–6Sn	2.7709	2.3807	4.17	12.22
Ti–3Nb–3Fe–4Sn	2.7748	2.3881	4.15	10.40
Ti–4Nb–3Fe–4Sn	2.7779	2.3879	4.16	10.80
Ti–6Nb–3Fe–4Sn	2.7841	2.3874	4.18	11.59
Ti–7Nb–3Fe–4Sn	2.7872	2.3872	4.19	11.98
Ti–8Nb–3Fe–4Sn	2.7903	2.3869	4.20	12.36
Ti–9Nb–3Fe–4Sn	2.7934	2.3867	4.21	12.73

2.2. Materials Preparation

Ti–5Nb–3Fe–(0–6)Sn and Ti–(3–9)Nb–3Fe–4Sn (at%) (hereafter all compositions are expressed in atomic percent) alloys were fabricated by an Ar arc-melting method using high-purity raw materials. During the melting process, each alloy ingot was inverted and remelted six times to ensure homogeneity of the composition. The weight change after melting was almost negligible, so the actual composition was considered to be the same as the nominal composition. The button-shaped arc melted ingots were homogenized at 1273 K for 7.2 ks in vacuum. Then, plates were cut from the homogenized button-shaped ingots using an electrodischarge machine and were encapsulated in a quartz tube in an Ar atmosphere and then solution-treated at 1273 K for 7.2 ks, followed by water quenching by breaking the quartz tube in water. The plates were then cold-rolled into sheets with a final reduction of 95%. The final thickness of all the cold-rolled sheets was approximately about 0.20 mm. The specimens for mechanical and microstructural evaluation such as tensile tests, Young's modulus measurements, and X-ray diffraction (XRD) measurements were cut along the rolling direction using an electrodischarge machine. The longitudinal direction of these specimens was strictly kept parallel to the rolling direction. Finally, the cold-rolled specimens were encapsulated in quartz tubes in an Ar atmosphere and were subjected to heat treatment at 1073 K for 1.8 ks and then were quenched in water by breaking the quartz tubes. Etching solution with the following chemical composition; $H_2O:HNO_3:HF = 5:4:1$(v/v/v) was used to remove the oxidized surface layer of the specimens.

2.3. Microstructural Analysis and Evaluation of Mechanical Properties

The phase constituents of the samples were investigated at room temperature using an XRD apparatus with Cu $K\alpha$ radiation operated at 40 kV and 40 mA. The three incomplete pole figures were obtained from the diffraction intensities of three main crystal planes, that is, $\{110\}_\beta$, $\{200\}_\beta$, and $\{211\}_\beta$ of the β phase. Orientation distribution functions (ODFs) were also constructed using the aforementioned three pole figures of the β phase. Microstructure observations were carried out using a scanning electron microscope (SEM) on a JEOL JSM-IT300 and a TSL/OIM electron backscatter diffraction (EBSD) attachment. Specimens for SEM observation were prepared by mechanical polishing with SiC sandpapers, followed by electrochemical polishing using a solution of $HClO_4:C_4H_{10}O:CH_3OH = 1:6:10$(v/v/v) at about 233 K. TEM observations were performed on a JEOL 2010 F instrument operated at 200 kV. Specimens for transmission electron microscopy (TEM) were prepared using a twin-jet polishing machine (TenuPol-3, Struers) with a solution of $HF:H_2SO_4:CH_3OH = 2:5:93$ (v/v/v) at about 233 K.

Mechanical properties were evaluated by performing tensile tests and Young's modulus measurements. Tensile tests were carried out at an initial strain rate of $3 \times 10^{-4}\,s^{-1}$ at room temperature using a tensile testing machine (AG-X, Shimadzu). The dimensions of the rectangular shaped tensile specimens were 0.20 mm in thickness and 1.5 mm in width, with a length of 40 mm. The tensile direction of the specimen was parallel to the rolling direction. Both ends of the tensile specimens were fixed with two chucks so that the gauge length was 20 mm and the strain of the specimens was determined by measuring the distance between the chucks using an extensometer. The Young's modulus values of the alloys were measured at room temperature using a standard free resonance vibration method by Nippon Techno-Plus Co. Ltd. (JE2-C1/TE2-RT) instrument. The dimensions of the specimens for measuring Young's modulus were 30 mm in length, 6 mm in width, and 0.20 mm in thickness. The direction of the Young's modulus measurements was also chosen to be parallel to the rolling direction.

3. Results

3.1. Phase Constitutions

Figure 2a,b shows the XRD profiles of Ti–5Nb–3Fe–(0–6)Sn and Ti–(3–9)Nb–3Fe–4Sn alloys heat treated at 1073 K for 1.8 ks, respectively. It is clearly seen that all the Ti–5Nb–3Fe–(0–6)Sn and Ti–(3–9)Nb–3Fe–4Sn alloys consist of only a single β phase. No peaks from the α'' phase and the ω phase were identified by XRD measurements. It is also noted that the peak intensities were changed by changing the Sn and Nb contents. For example, the intensity of the 110_β peak was significantly changed by the Sn content, as shown in Figure 2a. The Ti–5Nb–3Fe alloy exhibited a very weak 110_β peak; however, the intensity of the 110_β peak gradually became sharper with increasing Sn content from 0 to 5 at% and then decreased again with further addition of Sn. Similarly, the relative intensities of the peaks were varied by changing the Nb content as shown in Figure 2b. For example, the Ti–3Nb–3Fe–4Sn alloy exhibited a weak 110_β peak; however, the Ti–4Nb–3Fe–4Sn alloy exhibited a sharp and strong 110_β peak. Then the intensity of the 110_β peak gradually became weaker with increasing Nb content from 5 to 9 at%. It is supposed that this distinct trend of 110_β peak intensity with varying Sn and Nb contents is possibly due to the change of recrystallization texture in Ti–5Nb–3Fe–(0–6)Sn and Ti–(3–9)Nb–3Fe–4Sn alloys. The recrystallization texture of the alloys will be described in a later section.

3.2. Tensile Properties and Young's Modulus

Figure 3a shows tensile stress–strain curves of Ti–5Nb–3Fe–(0–6)Sn alloys heat treated at 1073 K for 1.8 ks. It is seen that mechanical properties are strongly influenced by the Sn content. The Ti–5Nb–3Fe alloy exhibited a distinguished work hardening, high tensile strength, and serrated stress flow behavior. A high ultimate tensile strength of 969 MPa and a large elongation of 20% were observed in the Ti–5Nb–3Fe alloy. As the Sn content increased, the work hardening rate was reduced, and then the alloys with higher Sn contents exhibited negligible work hardening. The ultimate tensile strength tended to decrease with the increase in Sn content as shown in **Figure 4**a. It is also noted that the slope of the elastic deformation region, which corresponds to Young's modulus, varies with the Sn content. Young's modulus was measured by resonance vibration method for the Ti–5Nb–3Fe–(0–6)Sn alloys, and the results are plotted against Sn content in Figure 4c. The Ti–5Nb–3Fe alloy exhibited a high Young's modulus of 94 GPa,

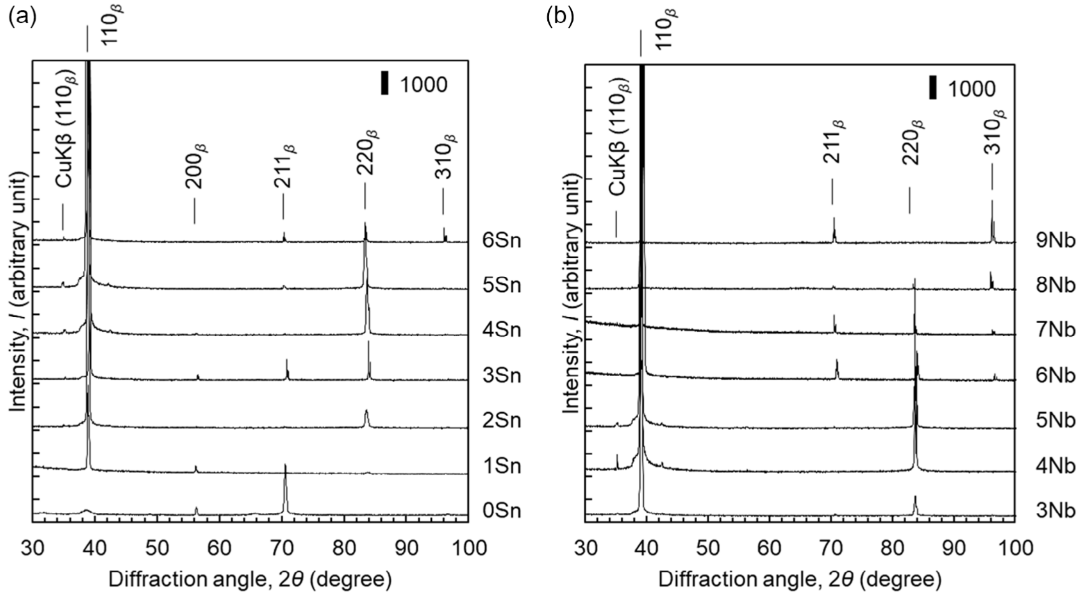

Figure 2. XRD patterns of a) Ti–5Nb–3Fe–(0–6)Sn and b) Ti–(3–9)Nb–3Fe–4Sn alloys heat treated at 1073 K for 1.8 ks.

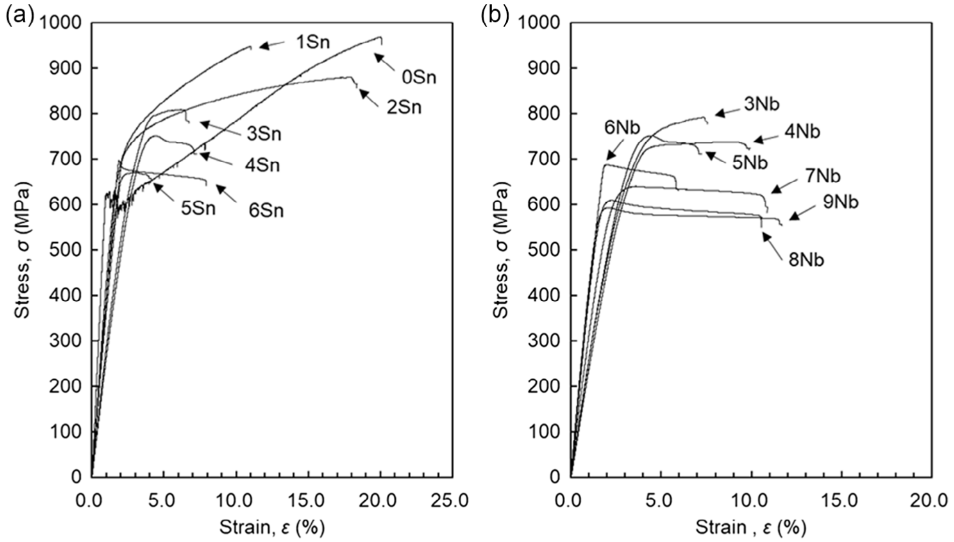

Figure 3. Stress–strain curves of a) Ti–5Nb–3Fe–(0–6)Sn and b) Ti–(3–9)Nb–3Fe–4Sn alloys.

and it decreased drastically with increasing Sn content up to 4 at%, and then increased again with further increasing Sn content. It is noted that the Ti–5Nb–3Fe–4Sn alloy exhibited an exceptionally low Young's modulus of 30 GPa with a high tensile strength of 750 MPa.

Stress–strain curves of Ti–(3–9)Nb–3Fe–4Sn alloys are shown in Figure 3b. Although the effect of Nb is weaker than that of Sn, the tensile strength and Young's modulus were influenced by the Nb content. The maximum tensile strength and Young's modulus are plotted against Nb content in Figure 4b,d, respectively. It is seen that the ultimate tensile strength tended to decrease with the increase of the Nb content. A low Young's modulus of 39 GPa was observed in the Ti–3Nb–3Fe–4Sn alloy, and it decreased with increasing Nb content. A minimum Young's modulus of 30 GPa was observed in the Ti–5Nb–3Fe–4Sn alloy, after which it increased with increasing Nb content.

3.3. Microstructural Analysis

In order to investigate the effect of the Sn content and Nb content on the microstructure, particularly on the athermal ω phase, TEM observation was carried out. **Figure 5** shows representative selected-area diffraction patterns along the zone axis $[113]_\beta$ and dark-field images obtained from a diffraction spot of the ω phase of Ti–5Nb–3Fe, Ti–5Nb–3Fe–2Sn, Ti–5Nb–3Fe–4Sn, and Ti–5Nb–3Fe–6Sn alloys. Diffraction spots from the β phase

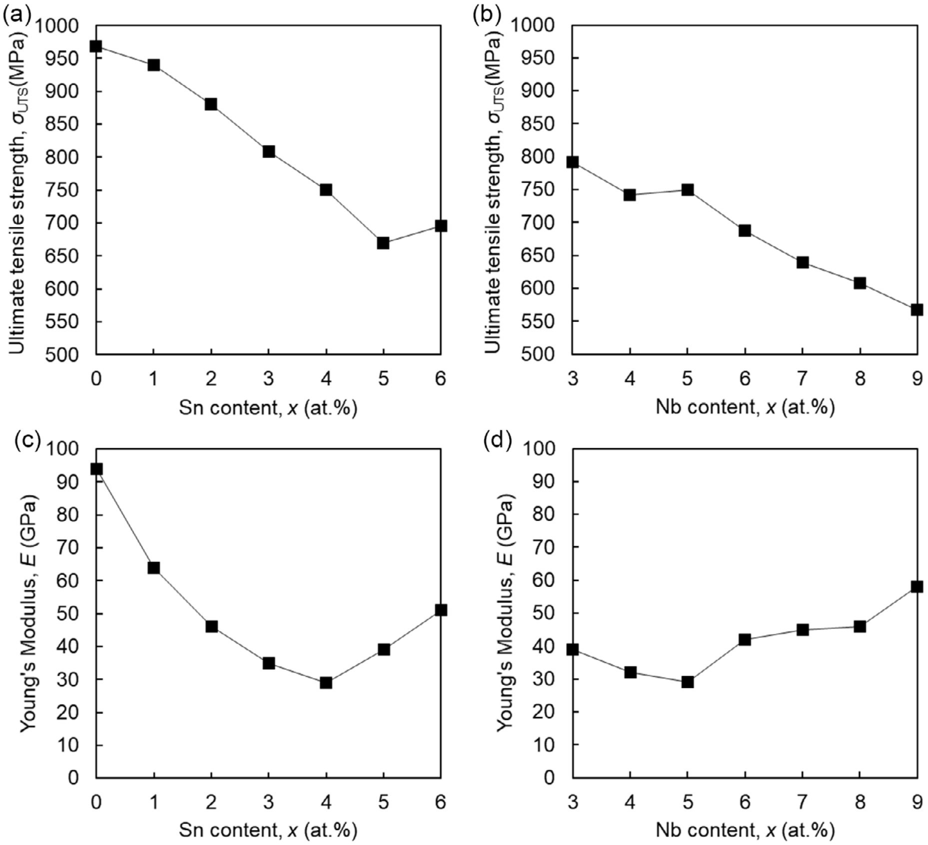

Figure 4. Ultimate tensile strength of a) Ti–5Nb–3Fe–(0–6)Sn and b) Ti–(3–9)Nb–3Fe–4Sn alloys and Young's modulus of c) Ti–5Nb–3Fe–(0–6)Sn and d) Ti–(3–9)Nb–3Fe–4Sn alloys.

were mainly observed in all the alloys. No additional spots from the α″ phase were observed, which is consistent with the XRD measurements as shown in Figure 2a. However, extra diffraction spots of the ω phase were clearly observed between the diffraction spots from the β phase in Ti–5Nb–3Fe, Ti–5Nb–3Fe–2Sn, and Ti–5Nb–3Fe–4Sn alloys, as shown in Figure 5a–c, respectively, revealing the formation of the athermal ω phase in all the alloys. It can be clearly seen that the size and volume fraction of the ω phase are dependent on Sn content. Diffraction spots of the ω phase of the Ti–5Nb–3Fe alloy were much stronger, and the corresponding dark-field image indicates that a large amount of ω phase was uniformly dispersed in the β phase matrix (as shown in Figure 5a). For the Ti–5Nb–3Fe–2Sn alloy, the intensity of the diffraction spots of the ω phase was relatively weak, and consequently the volume fraction of the ω phase in the corresponding dark-field image also decreased (as shown in Figure 5b). As the Sn content continued to increase, the intensity of the diffraction spots was further weakened. As a result, the size and volume fraction of the ω phase were reduced significantly in the Ti–5Nb–3Fe–4Sn alloy (as shown in Figure 5c). For the Ti–5Nb–3Fe–6Sn alloy, no distinct spot of the ω phase was detected. These results indicate that the quaternary addition of Sn is very useful in suppressing the tendency of the ω phase formation in the Ti–5Nb–3Fe alloy. This is corroborated by previous studies in which the addition of Sn suppresses the formation of the ω phase in metastable β-type alloys.[11,43,52–54]

Figure 6 shows selected-area diffraction patterns and dark-field images obtained from a diffraction spot of the ω phase for Ti–4Nb–3Fe–4Sn, Ti–5Nb–3Fe–4Sn, and Ti–6Nb–3Fe–4Sn alloys to exhibit the effect of Nb content on the formation of the ω phase. Diffraction spots of the ω phase were observed in all the diffraction patterns, indicating the presence of the athermal ω phase in all alloys. It is seen that the diffraction spots of the ω phase in the diffraction patterns became weaker and its volume fraction shown in dark-field images decreased with increasing Nb content. It is also noted that, comparing Figure 5 with Figure 6, Sn is considered to be more effective than Nb in suppressing the ω phase.

Figure 7 shows SEM micrographs of Ti–5Nb–3Fe–2Sn, Ti–5Nb–3Fe–4Sn, Ti–5Nb–3Fe–6Sn, Ti–4Nb–3Fe–4Sn, and Ti–6Nb–3Fe–4Sn alloys. All alloys consisted of single β phase with an equiaxed structure and the average grain size of the alloys was measured to be 51, 51, 54, 56, and 66 μm, respectively, indicating that there was little change in the grain size with the change of the Sn and Nb content. **Figure 8** shows the EBSD inverse pole figure (IPF) maps in the rolling direction (RD) and the normal direction to the rolling plane (ND) for the Ti–5Nb–3Fe–2Sn, Ti–5Nb–3Fe–4Sn, Ti–5Nb–3Fe–6Sn, Ti–4Nb–3Fe–4Sn, and Ti–6Nb–3Fe–4Sn alloys. From the IPF maps of the RD and ND, it is evident that the recrystallization texture was strongly dependent on the Sn and Nb content. The Ti–5Nb–3Fe–2Sn alloy exhibited a very strong $\{110\}_{\beta}<001>_{\beta}$

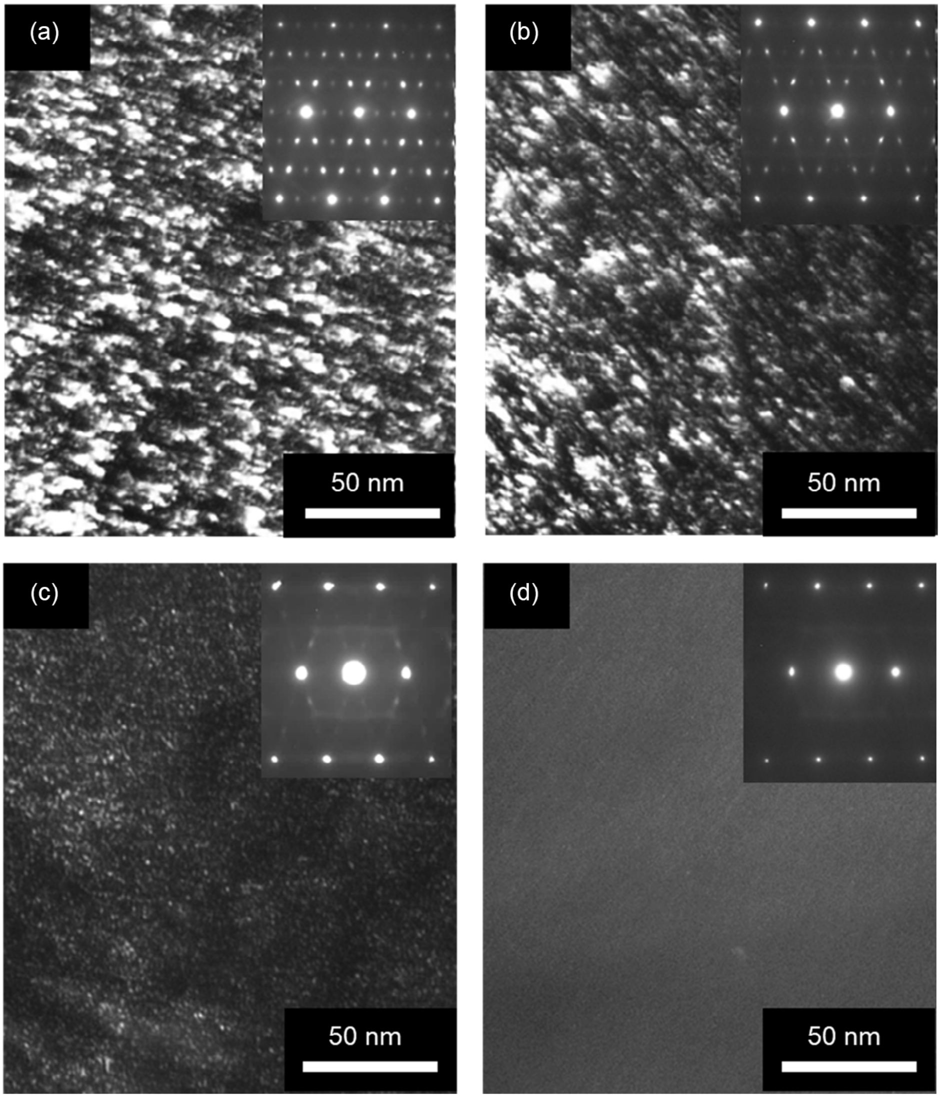

Figure 5. Selected-area diffraction patterns and dark-field images of the ω phase of a) Ti–5Nb–3Fe, b) Ti–5Nb–3Fe–2Sn, c) Ti–5Nb–3Fe–4Sn, and d) Ti–5Nb–3Fe–6Sn alloys.

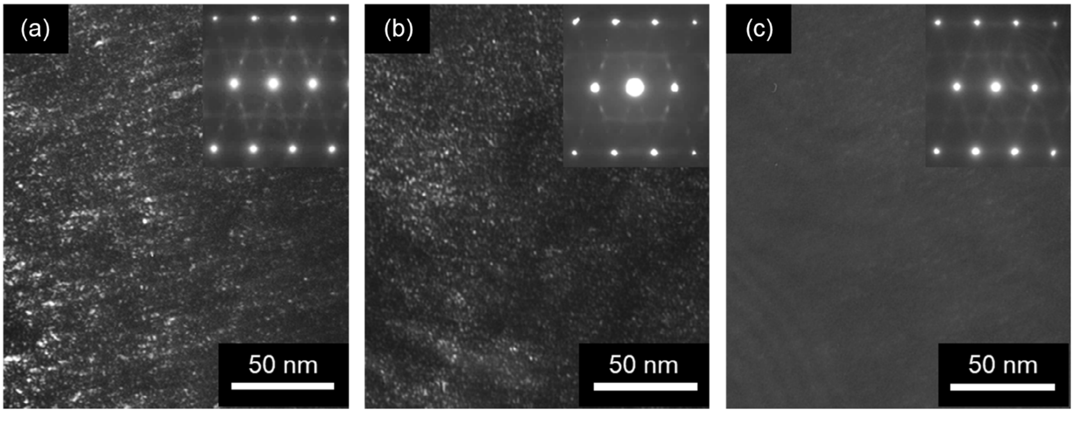

Figure 6. Selected-area diffraction patterns and dark-field images of the ω phase of a) Ti–4Nb–3Fe–4Sn, b) Ti–5Nb–3Fe–4Sn, and c) Ti–6Nb–3Fe–4Sn alloys.

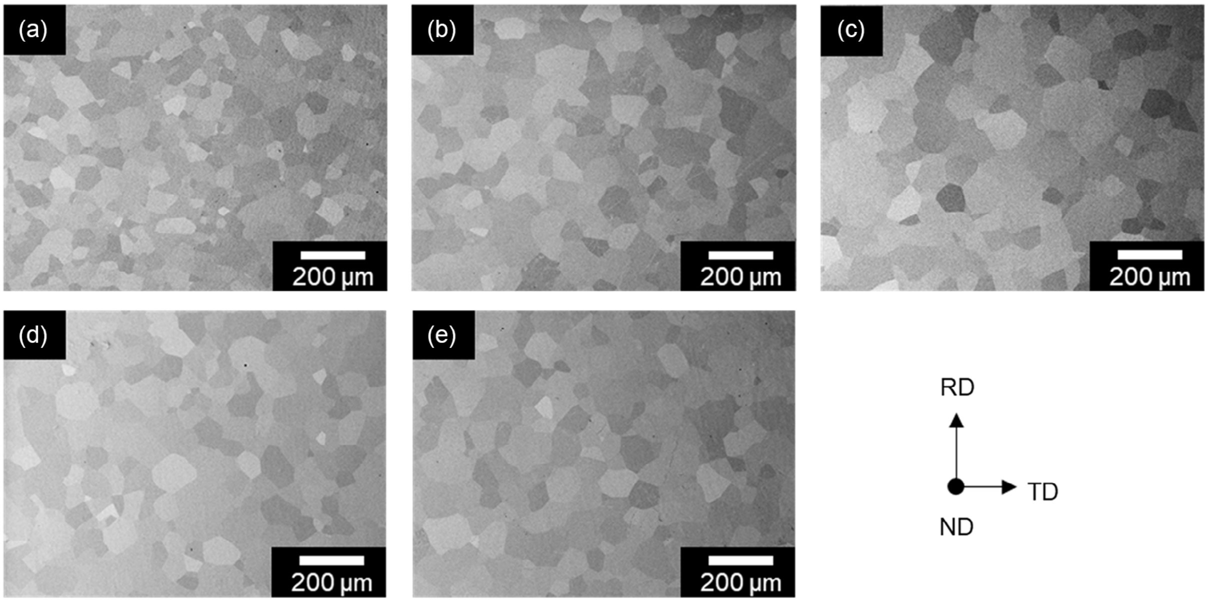

Figure 7. SEM micrographs of a) Ti–5Nb–3Fe–2Sn, b) Ti–5Nb–3Fe–4Sn, c) Ti–5Nb–3Fe–6Sn, d) Ti–4Nb–3Fe–4Sn, and e) Ti–6Nb–3Fe–4Sn alloys.

texture, which is known as the Goss texture. It is seen that the area fraction of Goss-oriented grains decreased with increasing Sn content as shown in Figure 8b,c. A strong $\{110\}_\beta<001>_\beta$ texture was also formed in the Ti–4Nb–3Fe–4Sn alloy but the Goss-oriented grains were not observed in the Ti–6Nb–3Fe–4Sn alloy as shown in Figure 8d,e.

3.4. Recrystallization Texture

To study the recrystallization texture quantitatively, the ODFs were calculated by measuring incomplete pole figures of three typical planes of $\{110\}_\beta$, $\{200\}_\beta$ and $\{211\}_\beta$ using XRD. **Figure 9** shows $\phi_2 = 45°$ sections of the ODFs obtained in Ti–5Nb–3Fe–(0–6)Sn alloys heat treated at 1073 K for 1.8 ks. The results clearly show a strong dependence of the recrystallization texture on Sn content. Figure 9a shows that the Ti–5Nb–3Fe alloy exhibited a very weak texture with a maximum intensity ($I_{\max}$) of 4 close to the $\{001\}_\beta<110>_\beta$ component. As the Sn content increased, the maximum intensity became stronger and the major component was changed to $\{110\}_\beta<001>_\beta$. The maximum orientation intensity at the $\{110\}_\beta<001>_\beta$ component became stronger with increasing Sn content, and the Ti–5Nb–3Fe–2Sn alloy revealed a very strong $\{110\}_\beta<001>_\beta$ texture with a maximum intensity ($I_{\max}$) of 82. With further increase in Sn content, the maximum orientation intensity of the $\{110\}_\beta<001>_\beta$ component became weaker and then no specific texture component was found in the Ti–5Nb–3Fe–6Sn alloy.

The recrystallization texture was also affected by the Nb content as shown in **Figure 10**. The $\{110\}_\beta<001>_\beta$ texture was observed in Ti–3Nb–3Fe–4Sn, Ti–4Nb–3Fe–4Sn, and Ti–5Nb–3Fe–4Sn alloys; the strongest intensity was observed in the Ti–4Nb–3Fe–4Sn alloy. The $\{110\}_\beta<001>_\beta$ component became very weak in the Ti–6Nb–3Fe–4Sn alloy, instead a weak γ-fiber texture with a maximum intensity at $\{111\}_\beta<110>_\beta$ was observed. No strong texture component was observed in the alloys with higher Nb content.

In metastable β-type Ti alloys, $\{112\}_\beta<110>_\beta$, $\{001\}_\beta<110>_\beta$, and γ-fiber texture have been reported as recrystallization textures. The $\{112\}_\beta<110>_\beta$ texture has been reported as a major recrystallization texture in metastable β-type Ti alloys, which have relatively high Nb content such as Ti–24Nb–3Al, Ti–22Nb–6Ta, Ti–35Nb–2Ta–3Zr (wt%), (Ti–35Nb)–4Sn (wt%), and (Ti–35Nb)–7.9Sn (wt%) alloys.[8,38,55,56] On the other hand, a strong $\{001\}_\beta<110>_\beta$ recrystallization texture has been reported in Ti–Zr–Nb–Sn-based alloys which have relatively low Nb content such as Ti–18Zr–11Nb–3Sn, Ti–20Zr–10Nb–3Sn, Ti–24Zr–10Nb–2Sn, and Ti–18Zr–4.5Nb–3Sn–2Mo alloys.[57–60] The effect of the Sn content on the recrystallization texture is also controversial. In this study, the intensity of the $\{110\}_\beta<001>_\beta$ texture increased with the addition of Sn up to 2 at%; however, the addition of 2%Sn mostly intensified the texture component of $\{001\}_\beta<110>_\beta$ in the Ti–18Zr–Nb–Sn system. The formation of Goss texture of $\{110\}_\beta<001>_\beta$ has been reported only in a few β-type Ti alloys such as Ti–Mo–Al–Zr, Ti–Zr–Nb–Sn–Mo, and Ti–Nb–Sn.[40–42] Although the cause of the change in recrystallization texture due to the change in Sn or Nb content is not clear at present, it is worth noting that the development of the $\{110\}_\beta<001>_\beta$ texture is very beneficial to achieve low Young's modulus because Young's modulus is minimized along the $<001>_\beta$ direction in β-type Ti alloys.

4. Discussion

It has been well established in previous studies that e/a is a dominant factor governing the phase stability and elastic constants of metastable β-type Ti alloys.[12,14,19,33–39] As e/a decreases, the β phase becomes unstable and hence Young's modulus decreases

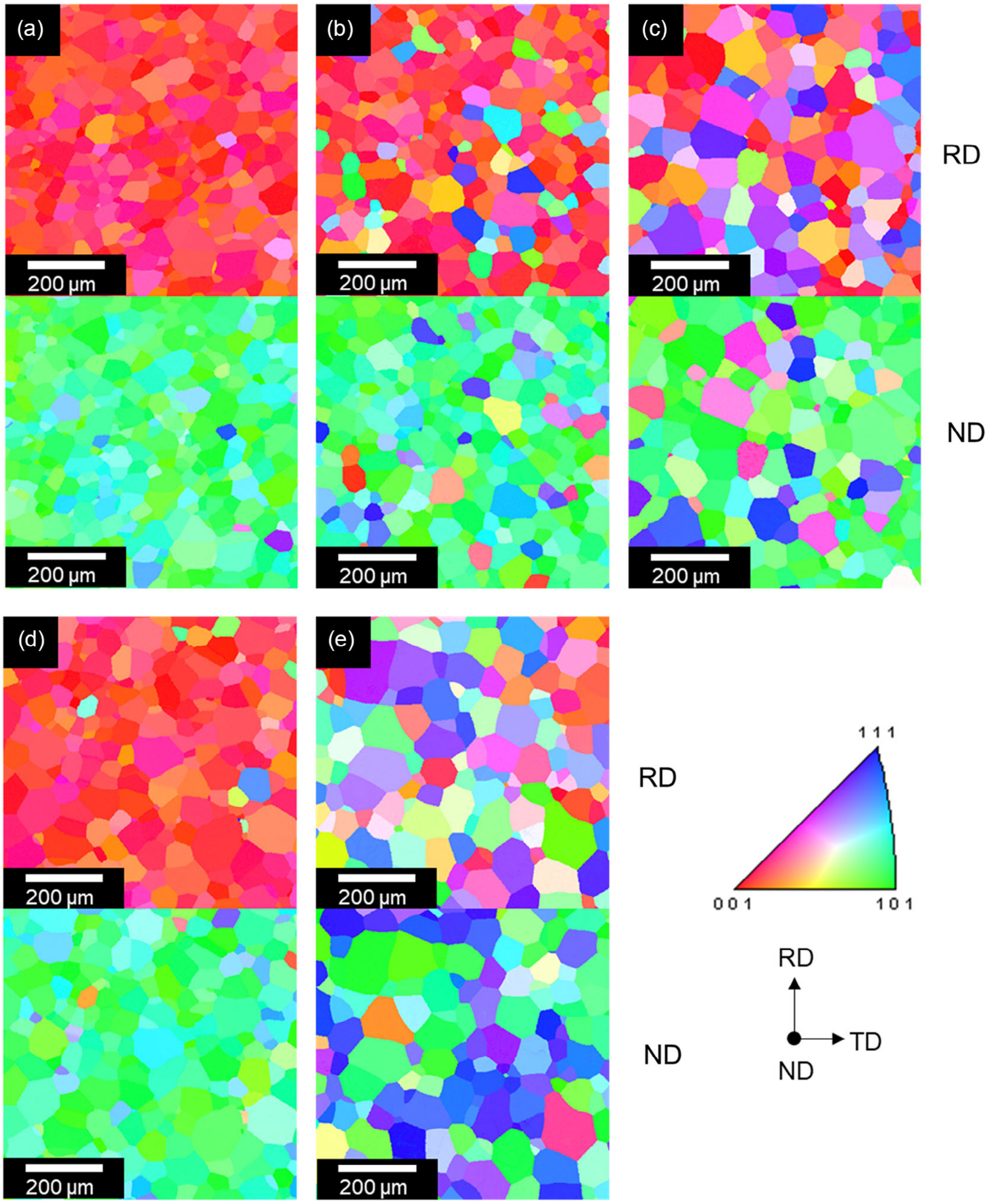

Figure 8. IPF maps of RD and ND directions of a) Ti–5Nb–3Fe–2Sn, b) Ti–5Nb–3Fe–4Sn, c) Ti–5Nb–3Fe–6Sn, d) Ti–4Nb–3Fe–4Sn, and e) Ti–6Nb–3Fe–4Sn alloys.

until the ω phase or the α″ martensite is formed. Therefore, Young's modulus exhibits a V-shaped or W-shaped dependence on e/a in metastable β-type Ti alloys. Young's modulus of the Ti–(3–9)Nb–3Fe–4Sn and Ti–5Nb–3Fe–(0–6)Sn alloys is plotted in **Figure 11**a as a function of e/a.

Figure 11a shows a V-shaped dependence of Young's modulus on e/a for the Ti–(3–9)Nb–3Fe–4Sn alloys. Young's modulus decreased with decreasing e/a until reaching a minimum value of 30 GPa at $e/a = 4.17$, that is, at the Ti–5Nb–3Fe–4Sn alloy, and then increased with further decreasing e/a. As shown in Figure 2b, no distinct peaks from α″ martensite phase were detected in the Ti–(3–9)Nb–3Fe–4Sn alloys. On the other hand, the diffraction intensity of the ω phase became strong with decreasing Nb content, although the intensity was weak, as shown in Figure 6, implying that the increase in volume fraction of the ω phase is one possible reason for the increase in Young's modulus at the compositions with lower Nb content. In addition, the Ti–(3–5)Nb–3Fe–4Sn alloys exhibited a strong $\{110\}_\beta\langle001\rangle_\beta$ texture, leading to a further decrease in Young's modulus. It is also interesting to note that the Ti–5Nb–3Fe–4Sn alloy exhibited

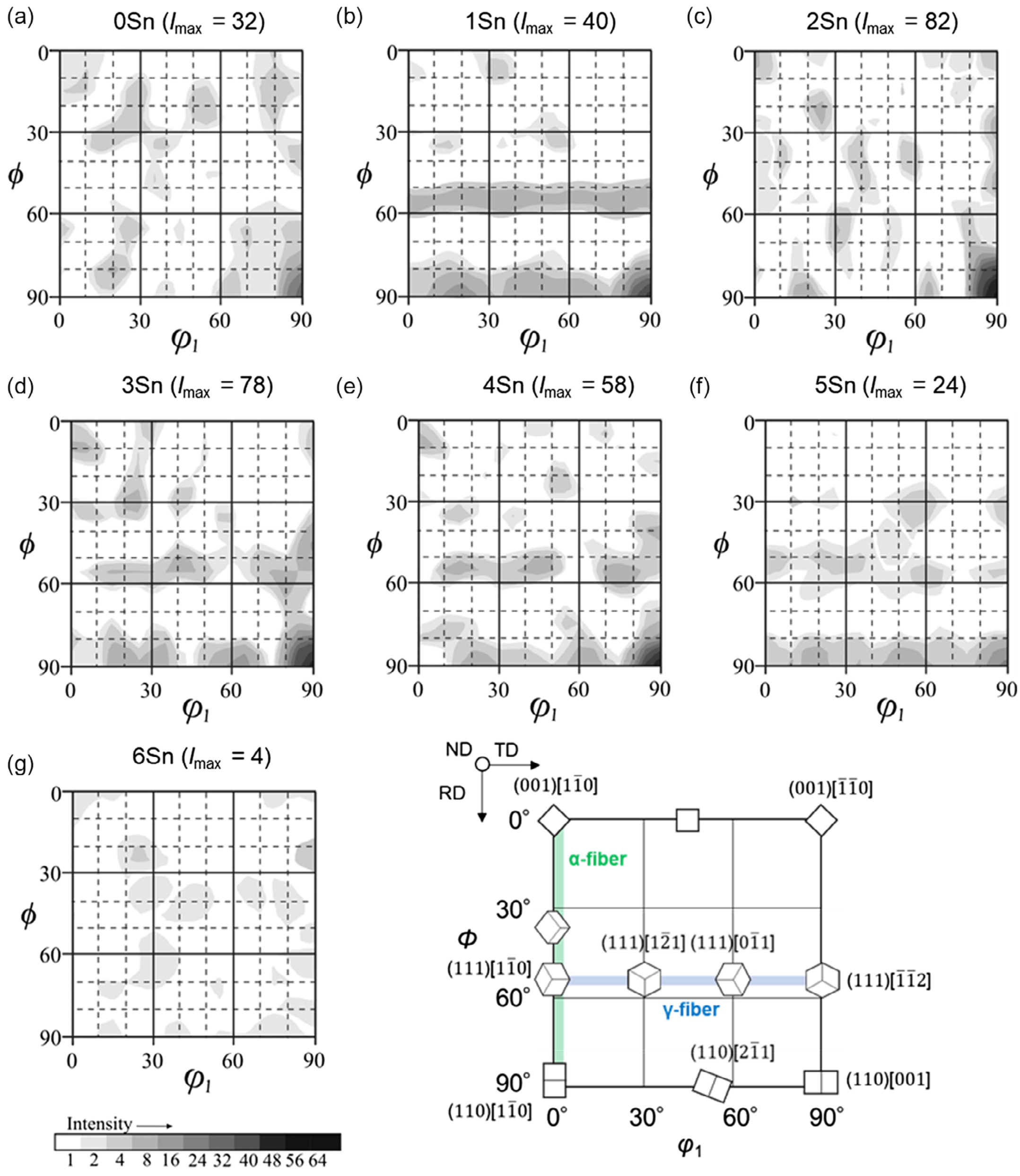

Figure 9. Sections ($\phi_2 = 45°$) of the ODFs of a) Ti–5Nb–3Fe, b) Ti–5Nb–3Fe–1Sn, c) Ti–5Nb–3Fe–2Sn, d) Ti–5Nb–3Fe–3Sn, e) Ti–5Nb–3Fe–4Sn, f) Ti–5Nb–3Fe–5Sn and g) Ti–5Nb–3Fe–6Sn alloys.

a lower Young's modulus compared with the Ti–4Nb–3Fe–4Sn alloy even though the $\{110\}_\beta\langle001\rangle_\beta$ texture was weaker in the Ti–5Nb–3Fe–4Sn alloy, implying that the effect of suppressing ω phase worked more strongly than the effect of $\{110\}_\beta\langle001\rangle_\beta$ texture.

On the other hand, it is noted that, even though the value of *e*/*a* was fixed, Young's modulus varied significantly in the range from 30 GPa to 94 GPa for the Ti–5Nb–3Fe–(0–6)Sn alloys. As shown in Figure 4c, Young's modulus shows a characteristic V-shaped dependence on the Sn content for the Ti–5Nb–3Fe–(0-6)Sn alloys. Young's modulus decreased with increasing Sn content, reached a minimum at 4 at% Sn, and then increased again. This Sn content dependence of Young's modulus can be described by the effects of Sn on the stability of the β phase and the ω phase. It has been well established that Sn affects the stability of the β phase; that is, Sn acts as a β phase stabilizing element relative to the α″ martensite phase although the addition of Sn does not change the *e*/*a* of the alloy.[8,10,11] In addition, it has been confirmed that the addition of Sn suppresses the formation of the athermal ω phase in Ti–Nb-based alloys. Consistent with previous studies, the athermal ω phase was remarkably reduced by the addition of Sn to the Ti–5Nb–3Fe alloy, as shown in Figure 5.[11,43,53,54] Therefore, it is supposed that the decrease in Young's modulus with

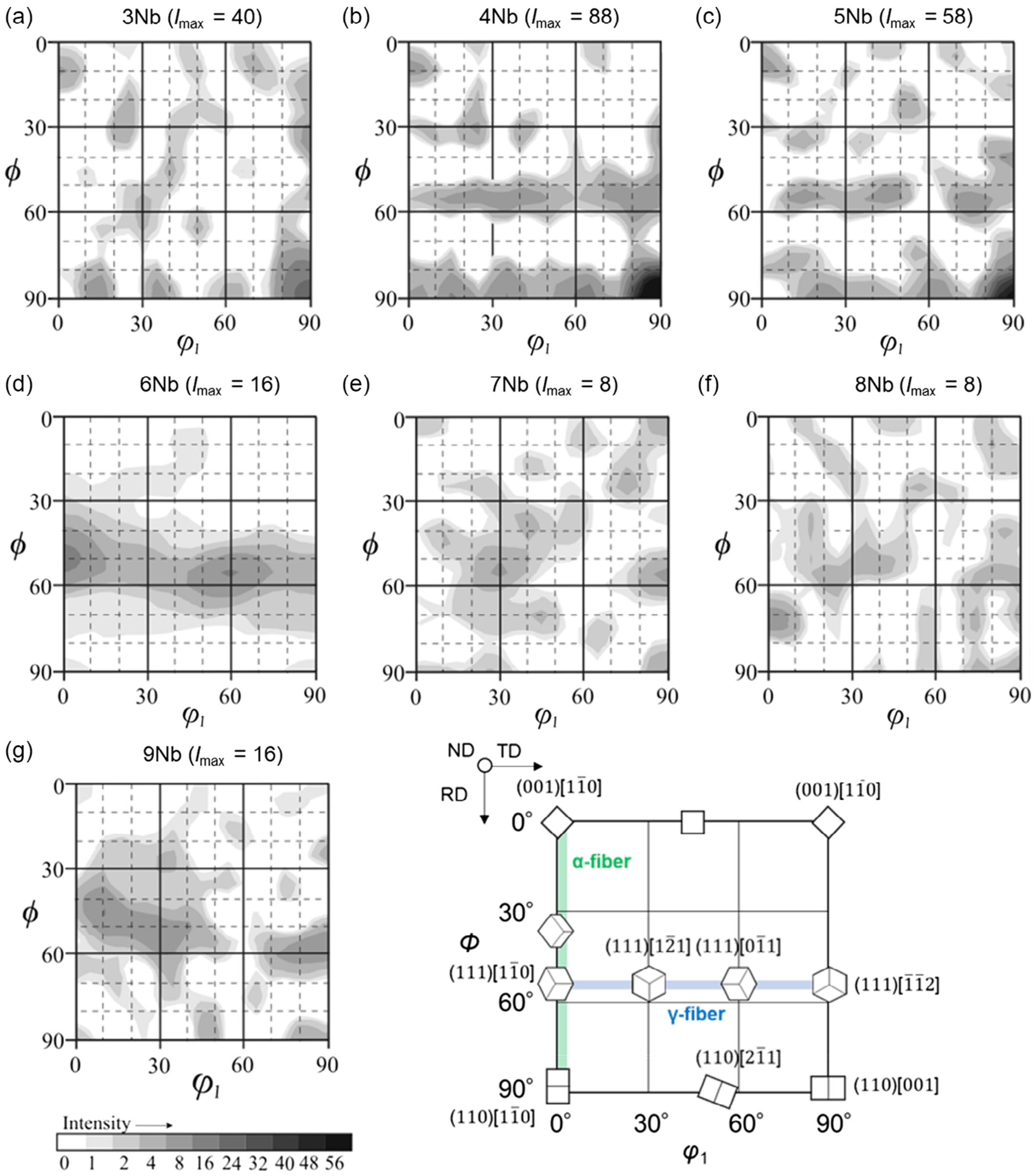

Figure 10. Sections ($\phi_2 = 45°$) of the ODFs of a) Ti–3Nb–3Fe–4Sn, b) Ti–4Nb–3Fe–4Sn, c) Ti–5Nb–3Fe–4Sn, d) Ti–6Nb–3Fe–4Sn, e) Ti–7Nb–3Fe–4Sn, f) Ti–8Nb–3Fe–4Sn and g) Ti–9Nb–3Fe–4Sn alloys.

increasing Sn content is due to the decrease in the athermal ω phase. Furthermore, the Ti–5Nb–3Fe–(2-4)Sn alloys exhibited a strong $\{110\}_\beta<001>_\beta$ texture. As a result, a very low Young's modulus of the Ti–5Nb–3Fe–4Sn alloy is supposed to be due to the combined effect of Sn in suppressing the athermal ω phase and forming the favorable recrystallization texture. In addition, it is noted that the Ti–5Nb–3Fe–2Sn alloy exhibited a higher Young's modulus than the Ti–4Nb–3Fe–4Sn alloy despite having a stronger $\{110\}_\beta<001>_\beta$ texture than the Ti–4Nb–3Fe–4Sn alloy, implying that the suppression of the athermal ω phase is more important in reducing Young's modulus.

The effect of Sn on Young's modulus is consistent with the previous study on Ti–15Nb–(4–6)Sn alloys.[42] Li et al. reported that a very low modulus of 31.5 GPa was achieved in a Ti–15Nb–5.5Sn alloy, which was attributed to the absence of the athermal ω phase and the formation of a strong $\{110\}_\beta<001>_\beta$ texture.[42] They also suggested that a modified Mo_{eq} proposed by Wang et al. was useful to assess the β phase stability of Sn-containing Ti alloys.[42,51] In Figure 11b, Young's modulus of the Ti–(3–9)Nb–3Fe–4Sn and Ti–5Nb–3Fe–(0–6)Sn alloys is plotted as a function of Mo_{eq}. It is seen that results of both series of alloys overlap each other and exhibit a clear V-shaped dependence of Young's modulus on Mo_{eq}, confirming that Mo_{eq} is a useful parameter to describe the composition dependence of mechanical properties for the Ti–(3–9)Nb–3Fe–4Sn and Ti–5Nb–3Fe–(0–6)Sn alloys. Young's

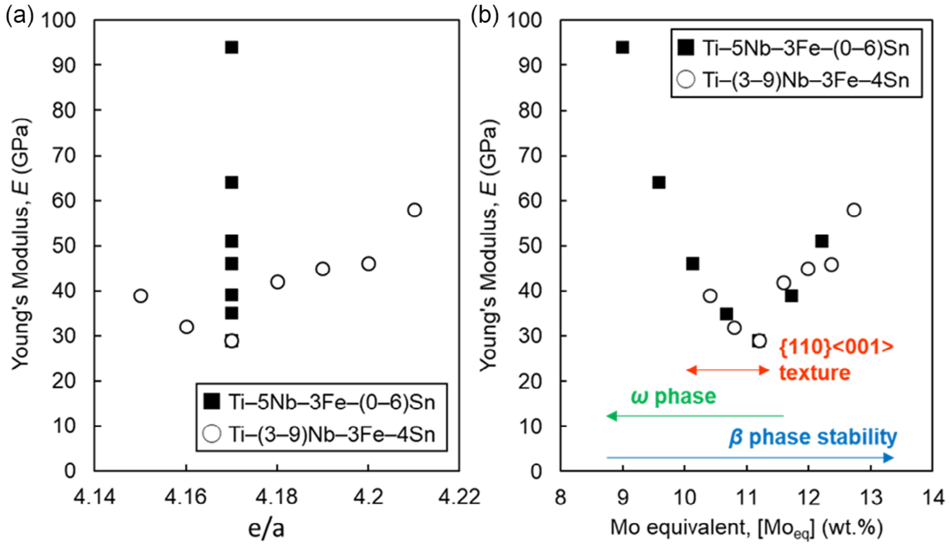

Figure 11. Young's modulus of Ti–5Nb–3Fe–(0-6)Sn and Ti–(3–9)Nb–3Fe–4Sn alloys plotted against a) e/a and b) Mo equivalent.

modulus decreased with increasing Mo$_{eq}$ reaching a minimum at Mo$_{eq}$ = 11.2 wt% and then increased again with further increasing Mo$_{eq}$. The composition dependence of Young's modulus is well described qualitatively by the β phase stability, athermal ω phase, and recrystallization texture. It is noted that, in both series of alloys, the changes in microstructure and recrystallization texture show almost the same trend with the change in Mo$_{eq}$; the amount of the athermal ω phase decreased with the increase in Mo$_{eq}$ and a strong $\{110\}_\beta\langle 001\rangle_\beta$ recrystallization texture was formed in the range of $10.1 \leq \text{Mo}_{eq} \leq 11.2$ for both series of alloys, although the formation mechanism remained unclear at this stage. Consequently, it is found that the minimum point is determined by the balance between the stability of the β phase, amount of the ω phase, and the recrystallization texture. The Ti–5Nb–3Fe–4Sn alloy exhibited an excellent combination of an ultralow Young's modulus of 30 GPa and a high tensile strength of 750 MPa in the solution-treated condition. In this study, the amount of Fe is fixed, but the amount of Fe can be an important parameter to control the stability of β-phase, microstructure, and mechanical properties. It is expected that changing the Fe content will affect the optimum content of Nb and Sn.

In addition to the alloy composition, microstructure and mechanical properties of metastable β-type Ti alloys are highly dependent on the thermomechanical process.[8,61–66] For example, annealing temperature and time are important parameters in controlling microstructure and mechanical properties. Matsumoto et al. investigated the microstructural changes during thermomechanical processing and the mechanical properties in a (Ti–35Nb)–4Sn (wt%) alloy.[8] They reported that a low-temperature annealing at 523 K for 7.2 ks after 89% cold rolling was effective in increasing tensile strength with keeping low Young's modulus due to the formation of fine microstructure. It has been reported that short time annealing is also effective to optimized the mechanical properties. For example. Elmay et al. reported that a low incipient elastic modulus (35 GPa) and a high strength (900 MPa) was achieved by short time annealing (0.6 ks) at 573 K after 95% cold rolling in a Ti–24Nb alloy due to a complex microstructure consisting of nanoscale (α+ω) phases in fine β grains.[61] Cold rolling ratio is also an important parameter because not only deformation texture but also recrystallization texture is strongly dependent on the deformation ratio.[62–64] Recently, it was suggested that Young's modulus of a Ti–13Nb–13Zr (wt%) alloy could be further reduced by a cold caliber rolling due to the formation of fine (α′+α″) structure.[65] This study focused on the effect of the Nb content and Sn content on the microstructure and mechanical properties using solution-treated specimens. It is expected that the mechanical performance of the designed alloy could be further enhanced by an optimal thermomechanical process.

5. Conclusion

Ti–Nb–Fe–Sn alloys with relatively low Nb contents were designed on the basis of electron–to-atom (e/a) ratio, d-electron alloy design concept, and Mo equivalent (Mo$_{eq}$) with the aim of achieving low Young's modulus comparable to human bone. The effect of Sn content and Nb content on the microstructure and the mechanical properties was investigated in Ti–5Nb–3Fe–(0–6) Sn (at%) and Ti–(3–9)Nb–3Fe–4Sn (at%) alloys heat treated at 1073 K for 1.8 ks. The main conclusions are as follows. 1) XRD measurements revealed that the Ti–5Nb–3Fe–(0–6)Sn and Ti–(3–9)Nb–3Fe–4Sn alloys consist of only a single β phase. The athermal ω phase was found to be formed in the Ti–5Nb–3Fe–(0–6)Sn and Ti–(3–9)Nb–3Fe–4Sn alloys by TEM observation. The addition of Sn suppressed the formation of the athermal ω phase. For the Ti–5Nb–3Fe–6Sn alloy, the ω phase was not detected. 2) The recrystallization texture was strongly affected not only by the Sn content but also by the Nb content. A strong $\{110\}_\beta\langle 001\rangle_\beta$ Goss texture was formed in the Ti–5Nb–3Fe–(2–4)Sn and Ti–(3–5)Nb–3Fe–4Sn alloys. 3) A high ultimate tensile strength of 969 MPa and a high Young's modulus of 94 GPa were observed in the Ti–5Nb–3Fe alloy. The ultimate tensile strength gradually decreased with increasing Sn content. Young's modulus decreased drastically with increasing Sn content up to 4 at% and then increased with further increasing Sn content. 4) For the Ti–(3–9)Nb–3Fe–4Sn alloys, the ultimate tensile strength tended to decrease with increasing Nb content. Young's modulus decreased with increasing Nb content up to 5 at% and then increased with further increasing Nb content. 5) The Ti–5Nb–3Fe–4Sn alloy exhibited an exceptionally low Young's modulus of 30 GPa with a high tensile strength of 750 MPa due to the combined effect of low stability of the β phase, small amount of ω phase, and strong $\{110\}_\beta\langle 001\rangle_\beta$ Goss texture.

Acknowledgements

This work was partially supported by Japan Society for the Promotion of Science (JSPS) KAKENHI grant numbers 21K14395 and 21H01647. The authors acknowledge to support by Iketani Science and Technology Foundation grant number 0331070-A.

Conflict of Interest

The authors declare no conflict of interest.

Data Availability Statement

The data that support the findings of this study are available from the corresponding author upon reasonable request.

Keywords

low elastic moduli, mechanical properties, textures, Ti alloys, Young's moduli

Received: April 4, 2023
Revised: June 19, 2023
Published online:

---

[1] M. Geetha, A. K. Singh, R. Asokamani, A. K. Gogia, *Prog. Mater. Sci.* **2009**, *54*, 397.
[2] M. Kaur, K. Singh, *Mater. Sci. Eng., C* **2019**, *102*, 844.
[3] M. Niinomi, *J. Mech. Behav. Biomed. Mater.* **2008**, *1*, 30.
[4] M. Niinomi, M. Nakai, J. Hieda, *Acta Biomater.* **2012**, *8*, 3888.
[5] Q. Chen, G. A. Thouas, *Mater. Sci. Eng., R* **2015**, *87*, 1.
[6] M. I. Z. Ridzwan, S. Shuib, A. Y. Hassan, A. A. Shokri, M. N. M. Ibrahim, *J. Med. Sci.* **2007**, *7*, 460.
[7] T. Saito, T. Furuta, J. H. Hwang, S. Kuramoto, K. Nishino, N. Suzuki, R. Chen, A. Yamada, K. Ito, Y. Seno, T. Nonaka, H. Ikehata, N. Nagasako, C. Iwamoto, Y. Ikuhara, T. Sakuma, *Science* **2003**, *300*, 464.
[8] H. Matsumoto, S. Watanabe, S. Hanada, *Mater. Trans.* **2005**, *46*, 1070.
[9] L. M. Elias, S. G. Schneider, S. Schneider, H. M. Silva, F. Malvisi, *Mater. Sci. Eng., A* **2006**, *432*, 108.
[10] H. Matsumoto, S. Watanabe, S. Hanada, *J. Alloys Compd.* **2007**, *439*, 146.
[11] Y. L. Hao, S. J. Li, S. Y. Sun, R. Yang, *Mater. Sci. Eng., A* **2006**, *441*, 112.
[12] Y. L. Hao, S. J. Li, S. Y. Sun, C. Y. Zheng, R. Yang, *Acta Biomater.* **2007**, *3*, 277.
[13] P. Laheurte, F. Prima, A. Eberhardt, T. Gloriant, M. Wary, E. Patoor, *J. Mech. Behav. Biomed. Mater.* **2010**, *3*, 565.
[14] M. Tane, S. Akita, T. Nakano, K. Hagihara, Y. Umakoshi, M. Niinomi, H. Mori, H. Nakajima, *Acta Mater.* **2010**, *58*, 6790.
[15] C. Ning, D. Ding, K. Dai, W. Zhai, L. Chen, *Biomed. Mater.* **2010**, *5*, 045006.
[16] X. Zhao, M. Niinomi, M. Nakai, T. Ishimoto, T. Nakano, *Mater. Sci. Eng., C* **2011**, *31*, 1436.
[17] K. Miura, N. Yamada, S. Hanada, T. K. Jung, E. Itoi, *Acta Biomater.* **2011**, *7*, 2320.
[18] M. Nakai, M. Niinomi, T. Oneda, *Metall. Mater. Trans. A* **2012**, *43*, 294.
[19] L. You, X. Song, *Scr. Mater.* **2012**, *67*, 57.
[20] Y. L. Hao, S. J. Li, F. Prima, R. Yang, *Scr. Mater.* **2012**, *67*, 487.
[21] M. González, J. Peña, F. J. Gil, J. M. Manero, *Mater. Sci. Eng., C* **2014**, *42*, 691.
[22] L. Hu, S. Guo, Q. Meng, X. Zhao, *Metall. Mater. Trans. A* **2014**, *45*, 547.
[23] S. Guo, Q. Meng, X. Zhao, Q. Wei, H. Xu, *Sci. Rep.* **2015**, *5*, 14688.
[24] S. Ozan, J. Lin, J. Ma, Y. Li, R. Ipek, C. Wen, *Acta Biomater.* **2015**, *20*, 176.
[25] S. Liang, X. Feng, L. Yin, X. Liu, M. Ma, R. Liu, *Mater. Sci. Eng., C* **2016**, *61*, 338.
[26] Y. P. Hou, S. Guoa, X. L. Qiao, T. Tian, Q. K. Meng, X. N. Cheng, X. Q. Zhao, *J. Mech. Behav. Biomed. Mater.* **2016**, *59*, 220.
[27] J. Málek, F. Hnilica, J. Veselý, B. Smola, K. Kolaˇrík, J. Fojt, M. Vlach, V. Kodetová, *Mater. Sci. Eng., A* **2016**, *675*, 1.
[28] Y. Shinohara, Y. Matsumoto, M. Tahara, H. Hosoda, T. Inamura, *Materialia* **2018**, *1*, 52.
[29] M. H. C. Tan, A. D. Baghi, R. Ghomashchi, W. Xiao, R. H. Oskouei, *J. Mech. Behav. Biomed. Mater.* **2019**, *99*, 78.
[30] K. M. Kim, H. Y. Kim, S. Miyazaki, *Materials* **2020**, *13*, 476.
[31] J. Fu, H. Y. Kim, S. Miyazaki, *Scr. Mater.* **2021**, *203*, 114068.
[32] V. Sheremetyev, K. Lukashevich, A. Kreitcberg, K. Kudryashova, M. Tsaturyants, S. Galkin, V. Andreev, S. Prokoshkin, V. Brailovski, *J. Alloys Compd.* **2022**, *928*, 167143.
[33] E. S. Fisher, D. Dever, *Acta Metall.* **1970**, *18*, 265.
[34] M. Tane, S. Akita, T. Nakano, K. Hagihara, Y. Umakoshi, M. Niinomi, H. Nakajima, *Acta Mater.* **2008**, *56*, 2856.
[35] D. Raabe, B. Sander, M. Friak, D. Ma, J. Neugebauer, *Acta Mater.* **2007**, *55*, 4475.
[36] X. Wang, L. Zhang, Z. Guo, Y. Jiang, X. Tao, L. Liu, *J. Mech. Behav. Biomed. Mater.* **2016**, *62*, 310.
[37] H. Y. Kim, S. Miyazaki, *Ni-Free Ti-Based Shape Memory Alloys*, Butterworth-Heinemann, Oxford, UK **2018**.
[38] T. Inamura, H. Hosoda, K. Wakashima, S. Miyazaki, *Mater. Trans.* **2005**, *46*, 1597.
[39] Y. W. Zhang, S. J. Li, E. G. Obbard, H. Wang, S. C. Wang, Y. L. Hao, R. Yang, *Acta Mater.* **2011**, *59*, 3081.
[40] Y. Shinohara, D. Narita, M. Tahara, H. Hosoda, T. Inamura, *Mater. Trans.* **2016**, *57*, 1998.
[41] K. M. Kim, Y. Al-Zain, A. Yamamoto, A. H. Daher, A. T. Mansour, J. M. AlAjlouni, A. S. Aloweidi, M. A. Al-Abbadi, H. Y. Kim, S. Miyazaki, *Adv. Eng. Mater.* **2021**, *24*, 2100776.
[42] S. Li, W. T. Lee, J. T. Yeom, J. G. Kim, J. S. Oh, T. Lee, Y. Liu, T. H. Nam, *J. Alloys Compd.* **2022**, *925*, 166724.
[43] Q. Li, T. Liu, J. Li, C. Cheng, M. Niinomi, K. Yamanaka, A. Chiba, T. Nakano, *J. Mater. Sci.* **2022**, *57*, 5634.
[44] M. R. Dal Bo, C. A. F. Salvador, M. G. Mello, D. D. Lima, G. A. Faria, A. J. Ramirez, R. Carama, *Mater. Des.* **2018**, *160*, 1186.
[45] C. A. F. Salvador, M. R. Dal Bo, D. D. Lima, C. R. Miranda, R. Caram, *J. Mater. Sci.* **2021**, *56*, 11494.

[46] C. D. Rabadia, Y. J. Liu, G. H. Cao, Y. H. Li, C. W. Zhang, T. B. Sercombe, H. Sun, L. C. Zhang, *Mater. Sci. Eng., A* **2018**, *732*, 368.
[47] M. Morinaga, N. Yukawa, T. Maya, K. Sone, H. Adach, in *Proc. Sixth World Conf. Titanium*, Cannes, France **1988**, p. 1601.
[48] M. Abdel-Hady, K. Hinoshita, M. Morinaga, *Scr. Mater.* **2006**, *55*, 477.
[49] M. Abdel-Hady, H. Fuwa, K. Hinoshita, H. Kimura, Y. Shinzato, M. Morinaga, *Scr. Mater.* **2007**, *57*, 1000.
[50] S. Sadeghpour, S. M. Abbasi, M. Morakabati, A. Kisko, L. P. Karjalainen, D. A. Porter, *J. Alloys Compd.* **2018**, *746*, 206.
[51] Q. Wang, C. Dong, P. K. Liaw, *Metall. Mater. Trans. A* **2015**, *46*, 3440.
[52] H. Y. Kim, T. Fukushima, P. J. S. Buenconsejo, T. H. Nam, S. Miyazaki, *Mater. Sci. Eng., A* **2011**, *528*, 7238.
[53] Y. Al-Zain, Y. Sato, H. Y. Kim, H. Hosoda, T. H. Nam, S. Miyazaki, *Acta Mater.* **2012**, *60*, 2437.
[54] M. F. Ijaz, H. Y. Kim, H. Hosoda, S. Miyazaki, *Scr. Mater.* **2014**, *72–73*, 29.
[55] H. Y. Kim, T. Sasaki, K. Okutsu, J. I. Kim, T. Inamura, H. Hosoda, S. Miyazaki, *Acta Mater.* **2006**, *54*, 423.
[56] L. Q. Wang, W. J. Lu, J. N. Qin, F. Zhang, D. Zhang, *Mater. Charact.* **2010**, *61*, 535.
[57] J. Fu, A. Yamamoto, H. Y. Kim, H. Hosoda, S. Miyazaki, *Acta Biomater.* **2015**, *17*, 56.
[58] S. Li, J. H. Lim, I. U. Rehman, W. T. Lee, J. G. Kim, J. S. Oh, T. Lee, T. H. Nam, *Mater. Sci. Eng., A* **2022**, *845*, 143243.
[59] L. L. Pavon, H. Y. Kim, H. Hosoda, S. Miyazaki, *Scr. Mater.* **2015**, *95*, 46.
[60] J. Fu, H. Y. Kim, S. Miyazaki, *J. Mech. Behav. Biomed. Mater.* **2017**, *65*, 716.
[61] W. Elmay, F. Prima, T. Gloriant, B. Bolle, Y. Zhong, E. Patoor, P. Laheurte, *J. Mech. Behav. Biomed. Mater.* **2013**, *18*, 47.
[62] T. Inamura, R. Shimizu, H. Y. Kim, S. Miyazaki, H. Hosoda, *Mater. Sci. Eng. C* **2016**, *61*, 499.
[63] A. Gupta, R. Khatirkar, J. Singh, *J. Alloys Compd.* **2022**, *899*, 163242.
[64] A. R. V. Nunes, S. Borborema, L. S. Araujo, L. Malet, J. Dille, L. H. de Almeida, *J. Alloys Compd.* **2020**, *820*, 153078.
[65] T. Lee, S. Lee, I. S. Kim, Y. H. Moon, H. S. Kim, C. H. Park, *J. Alloys Compd.* **2020**, *828*, 154401.
[66] P. A. B. Kuroda, M. L. Lourenço, D. R. N. Correa, C. R. Grandini, *J. Alloys Compd.* **2020**, *812*, 152108.